



# Quantification of double-layer Ni/YSZ fuel cell anodes from focused ion beam tomography data



Jochen Joos<sup>a,\*</sup>, Moses Ender<sup>a</sup>, Ingo Rotscholl<sup>a</sup>, Norbert H. Menzler<sup>b</sup>, Ellen Ivers-Tiffée<sup>a,1</sup>

<sup>a</sup> Karlsruhe Institute of Technology (KIT), Institut für Werkstoffe der Elektrotechnik (IWE), Adenauerring 20b, D-76131 Karlsruhe, Germany

<sup>b</sup> Forschungszentrum Jülich GmbH, Institute of Energy and Climate Research (IEK-1), D-52425 Jülich, Germany

## HIGHLIGHTS

- A new algorithm for the distinction between Ni-, YSZ-, and pore-phase is presented.
- 2 types of Ni/YSZ anodes are reconstructed and compared to each other.
- Microstructure parameters and particle size distributions are evaluated and discussed.
- The anode functional layer (AFL) adjacent to the electrolyte is separately quantified for the first time.
- Differences between both anode types and between AFL and substrates are discussed.

## ARTICLE INFO

### Article history:

Received 16 April 2013

Received in revised form

25 July 2013

Accepted 6 August 2013

Available online 20 August 2013

### Keywords:

SOFC

Ni/YSZ anode

Focused ion beam (FIB)

Microstructure reconstruction

Segmentation algorithm

Voxel

## ABSTRACT

Three-dimensional microstructure reconstructions of Ni–yttria-stabilized zirconia (Ni/YSZ) anodes are presented, all of which are based on focused ion beam tomography data.

The reconstruction procedure, starting from a series of 2D scanning electron micrographs, is investigated step by step and potential sources of error are identified. The distinction between Ni phase, YSZ phase and pore phase is solved by an advanced algorithm, which belongs to the *region-growing* image segmentation methods. This improves the accuracy of automated grayscale segmentation especially for images with low contrast, which is characteristic of both solid phases in Ni/YSZ anodes.

Critical microstructure parameters like material fractions, surface areas, particle size and distribution of Ni, YSZ, and pore phase, as well as phase connectivity and triple-phase boundary density, are evaluated and discussed.

In this contribution, two types of high-performance Ni/YSZ anodes – differing in thickness of both the anode functional layer and the anode substrate – are reconstructed and compared to each other. For the first time, the anode functional layer adjacent to the thin film electrolyte is separately quantified. The presented methods are qualified to quantitatively compare different anode microstructures and relate the result to their electrochemical performance.

© 2013 Elsevier B.V. All rights reserved.

## 1. Introduction

Solid oxide fuel cells (SOFCs) are one of the most promising energy conversion technologies due to their high efficiency, low emissions and fuel flexibility. The electrochemically active part of an SOFC consists of three components: two porous electrodes (anode and cathode), which are separated by a dense electrolyte [1]. Today, the state-of-the-art design is based on an anode-

supported cell (ASC) made of Ni and yttria-stabilized-zirconia (Ni/YSZ), developed for operating temperatures  $T_{op}$  of between 600 °C and 900 °C. High performance ASCs normally consist of a double-layer anode, (1) a 200–1500 µm thick and highly porous anode substrate – which provides mechanical stability and the transport of fuel, exhaust gases and electrons –, and, (2), a 5–30 µm thin anode functional layer (AFL) – which provides the electro-oxidation of the fuel (or the reduction of H<sub>2</sub>O and CO<sub>2</sub> in electrolysis mode) at the triple-phase boundary. Naturally, phase composition and microstructure of both layers have to be customized to the desired functionality. Hence, a separate quantification of the anode substrate and the AFL is a prerequisite for ASC improvement. Nonetheless, to the best of our knowledge, such an analysis using FIB tomography was not yet reported in literature.

\* Corresponding author. Tel.: +49 721 60847494; fax: +49 721 60847492.

E-mail address: [jochen.joos@kit.edu](mailto:jochen.joos@kit.edu) (J. Joos).

<sup>1</sup> DFG Center for Functional Nanostructures (CFN), Karlsruhe Institute of Technology (KIT), D-76131 Karlsruhe, Germany.

As stated above, the standard SOFC anode is a composite of three phases: (1) an electronic conducting solid (e.g. Ni), (2) an ionic conducting solid (e.g. YSZ) and (3) a pore phase. The oxidation of the fuel gas (e.g. H<sub>2</sub>) occurs, according to the following reaction:



Thus, the oxidation of the fuel gas requires a triple-phase boundary (TPB), where all three phases coexist. Moreover, an intimate contact between the two solid phases is required, and the electronic conducting phase must percolate with the current collector, the ionic conducting phase with the electrolyte and the pore phase with the gas channel.

This underlines microstructure as a key property [2,3], and improvement requires a quantification of the structural parameters and a correlation to their effects on electrochemical performance. Many groups have studied the subject of 3D reconstruction for SOFC anodes, and Table 1 lists available information (the list is far from exhaustive). Fig. 1 demonstrates, that reconstructed anode volumes start from 75  $\mu\text{m}^3$  [4] and go as large as 17,400  $\mu\text{m}^3$  [5], while the resolution can be as low as 4300 voxel per  $\mu\text{m}^3$  [5] or as high as 166,000 voxel per  $\mu\text{m}^3$  [6]. Naturally an appropriate resolution as well as a large enough volume is necessary to obtain reliable results, and hence a trade-off between resolution and volume is of particular importance. Sometimes, however, this high resolution was drastically downsized for the 3D simulation itself [7,8], most probably because of a lack of capable data handling software. This overview reveals, that both focused ion beam/scanning electron microscopy (FIB/SEM) (e.g. Refs. [4–15]) as well as X-ray (e.g. Refs. [16,17]) tomography methods were already applied to (i) quantify the structural parameters of SOFC anodes (e.g. Refs. [4,7,9–11,16]) or (ii) to implement 3D reconstruction data as model geometry in microstructure models (e.g. Refs. [5,6,8,9,18,19]). On the whole, much less information is available on the consecutive image processing steps, which are necessary to obtain reliable results based on high-quality tomography data. For example, the grayscale images, which consist of a voxel grid (voxel = volumetric

pixel), have to be partitioned into disjoint regions corresponding to the different phases in a segmentation procedure. This step is highly nontrivial, especially for microstructures with more than two phases, e.g., for solid oxide fuel cell anodes consisting of Ni phase, YSZ phase and pore phase. In the literature given in Table 1 and Fig. 1, the segmentation procedure was either done by hand [7,12] or semi-automatically [9,10], or reported as “grey level-based thresholding” [11] and based on “brightness of image” [13].

Jorgensen et al. [20] as well as Holzer et al. [21] presented advanced segmentation methods, but despite from that, not much is reported on the segmentation of SOFC anodes. In this contribution we introduce a fully automatable and precise multi-step segmentation procedure, which belongs to the *region-growing* image segmentation method [22] and demonstrate that the most common method of segmentation, thresholding [23], is inappropriate.

For this purpose, two different types of Ni/YSZ anodes, originating from high-performance anode-supported cells (ASC), are reconstructed via FIB-tomography. For the first time, both layers (anode substrate and anode functional layer) of an ASC are separately analyzed and compared with each other. For the sake of completeness, reconstruction data of a double-layer anode sintered onto an electrolyte supported (half) cell (ESC) is reported in Ref. [24]. Critical microstructure parameters like material fractions, surface areas, particle size distribution of Ni, YSZ, and pore phase, as well as phase connectivity and triple-phase boundary density, are evaluated and discussed.

## 2. Experimental

Two different types of anode-supported cells (ASCs) (herein referred to as type A and type B, respectively) are investigated. The ASCs have a double-layer anode, an anode functional layer and an anode substrate, using (1) nickel (Ni) as catalyst and electronic conducting solid, (2) yttria-stabilized zirconia (8YSZ) as ionic conducting solid, and, (3) a pore phase. The AFL has an interface to the thin ( $\sim 7$ – $10 \mu\text{m}$ ) 8YSZ electrolyte, which then is coated by a thin  $\text{Ce}_{0.8}\text{Gd}_{0.2}\text{O}_{2-\delta}$  (CGO) interlayer and a mixed ionic–electronic

**Table 1**

3D reconstructions of solid oxide fuel cell anodes, performed via FIB- and X-ray tomography, published in literature (the list is far from exhaustive).

Name	[Citation]/data set	Volume [ $\mu\text{m}^3$ ]	Pixel size [nm]	Image dist. [nm]	No. images [–]	No. voxel [ $\times 10^6$ ]
FIB tomography:						
Joos (this work)	Type A	1765	30	30	277	$\sim 65.36$
	Type B	887	30	30	149	$\sim 32.85$
Shearing	[4]/a	75	19	30	40	$\sim 6.9$
	[4]/b	722	20	19	175	$\sim 95$
Kanno	[5]/A	2424	37.2	74.5	n/a	$\sim 23.5$
	[5]/B	3905	37.2	61.7	n/a	$\sim 45.7$
	[5]/C	17,399	55.8	74.7	n/a	$\sim 74.8$
Shearing	[6]	50.6	20	15	100	$\sim 8.4$
Wilson	[7]	109	13.9	50	82	$\sim 12.8$
Matsuzaki	[8]	3391	13.7	59.2	228	$\sim 305.2$
Shikazono, Iwai	[9,10]	972	26	62	100	$\sim 23.2$
Vivet	[11]	967	10.4–13.2	100	115	$\sim 7.0$
Cronin	[12]/A	914	25	50	n/a	$\sim 29.2$
	[12]/B	1121	25	50	n/a	$\sim 35.9$
Kishimoto	[13]/A	1205	26.6	60	76	$\sim 28.4$
	[13]/B	1013	26.6	62	100	$\sim 23.1$
	[13]/C	1664	26.5	72	84	$\sim 32.9$
Matsui	[14]/Ini	1357	44.67	104.9	96	$\sim 6.5$
	[14]/A	1402	44.67	103.7	100	$\sim 6.8$
	[14]/B	1310	44.67	97.2	100	$\sim 6.8$
Matsui	[15]/1	3368	27.9	$\sim 61$	213	$\sim 71$
	[15]/2	3150	27.9	$\sim 61$	191	$\sim 66.6$
X-ray tomography:						
Laurencin	[16]	185,220	60	X-ray	X-ray	857.5
Shearing	[17]/200 $\times$	37,945	65	X-ray	X-ray	n/a
	[17]/800 $\times$	331	32	X-ray	X-ray	$\sim 10.1$

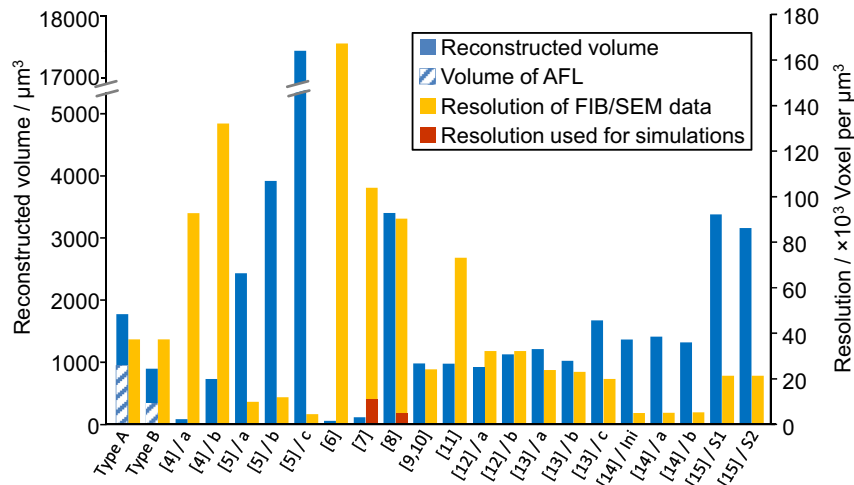


**Fig. 1.** Reconstructed volume (blue) and resolution (number of voxels per  $\mu\text{m}^3$ ) of reconstructed anodes published in literature (the list is far from exhaustive). (For interpretation of the references to color in this figure legend, the reader is referred to the web version of this article.)

conducting  $\text{La}_{0.58}\text{Sr}_{0.4}\text{Co}_{0.2}\text{Fe}_{0.8}\text{O}_{3-\delta}$  (LSCF) cathode. The double-layer anodes had a cross-sectional area of  $50 \times 50 \text{ mm}^2$ , which are entirely covered by the thin-film electrolyte. The active area of the working cathode was  $10 \times 10 \text{ mm}^2$ ; the cell geometry can be seen in Fig. 2.

Both ASCs were operated in the same test bench. A standard weight of 200 g was placed on top of the active cathode area. The reduction of NiO to Ni was performed at  $800^\circ\text{C}$  by a stepwise change of fuel composition from 100%  $\text{N}_2$  to 100%  $\text{H}_2$  and several hours of settling time.

Fig. 3 shows three SEM cross-section images of type A cell at different magnifications. Fig. 3a presents all layers, starting at the top with the LSCF cathode, followed by GCO interlayer (porous section) and YSZ electrolyte (dense section), the adjacent AFL and at the bottom the highly porous anode substrate. By using an in-lens detector the two solid phases Ni (white) and 8YSZ (gray) and the pore phase (black) are easily distinguishable. Figs. 3b and 2c are at higher magnifications, reveal the interface electrolyte/AFL and give details of the anode substrate. The in-lens detector allows us to distinguish the three phases herein; optical inspection clearly indicates that the microstructure of the anode substrate differs from the AFL.

Although both ASCs consist of the same materials, the double-layer anodes differ in structure and thickness. Fig. 4 shows SEM images of cross sections of type A and type B, taken during FIB processing. Type A has an anode substrate of  $1500 \mu\text{m}$  and an AFL of

$12 \mu\text{m}$ , whereas type B has an anode substrate of  $500 \mu\text{m}$  and an AFL of  $7 \mu\text{m}$ . As can already be seen by visual inspection of the cross section images, the microstructures of both layers differ as well. SEM images were taken after different (past) histories of the ASCs, which are listed in Table 2.

Although the evaluation of the electrical performance is beyond the scope of this study, it should be noted that ASC type A was evaluated by our group in great detail via electrochemical impedance spectroscopy and its characteristics features are published in Refs. [25–27].

## 2.1. Sample preparation

For further FIB/SEM treatment, the samples were prepared similarly to the preparation described in Refs. [19,28]. In order to easily identify the porous phase and distinguish it from the solid phases, the open porosity was infiltrated under vacuum conditions with an epoxy resin (Epofix, Struers). The cured samples were cut to a size of approximately  $3 \times 4 \times 6 \text{ mm}^3$  and finished by grinding and polishing to obtain planar surfaces and sharp edges. This allowed us to start the process of FIB sectioning right from the edge of the sample and – in combination with milling a trench left and right on the volume of interest – minimized shadowing effects. The sample was first tilted at  $90^\circ$  in order to mill a perfect planar surface on the top of the volume of interest. Together with the thin gold coating layer ( $\sim 100$ – $200 \text{ nm}$ ), which was sputter-coated on top of the sample to protect the surface and avoid electrical charging, this method produces sharp edges for the individual images and helps to reduce streaking. Fiducial marks on top provide control of slice alignment.

## 2.2. FIB/SEM observation

In this study a ZEISS 1540XB CrossBeam (Carl Zeiss AG, Oberkochen, Germany) was used to obtain cross-sectional images of the anode, containing the anode/electrolyte interface, the AFL and a part of the anode substrate adjacent to the AFL. Naturally, the quality of the reconstruction and hence of the calculated microstructure parameters depends on a high quality of image data. Furthermore, the observed volume must be sufficiently large to be statistically representative of the whole structure [28,29]. For the two types of anodes, several hundreds of consecutive images were collected during the automated procedure of sequential FIB milling

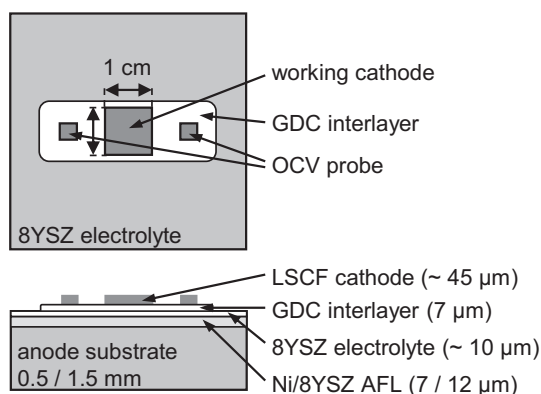


**Fig. 2.** ASC cell design: top view and side view (not to scale).

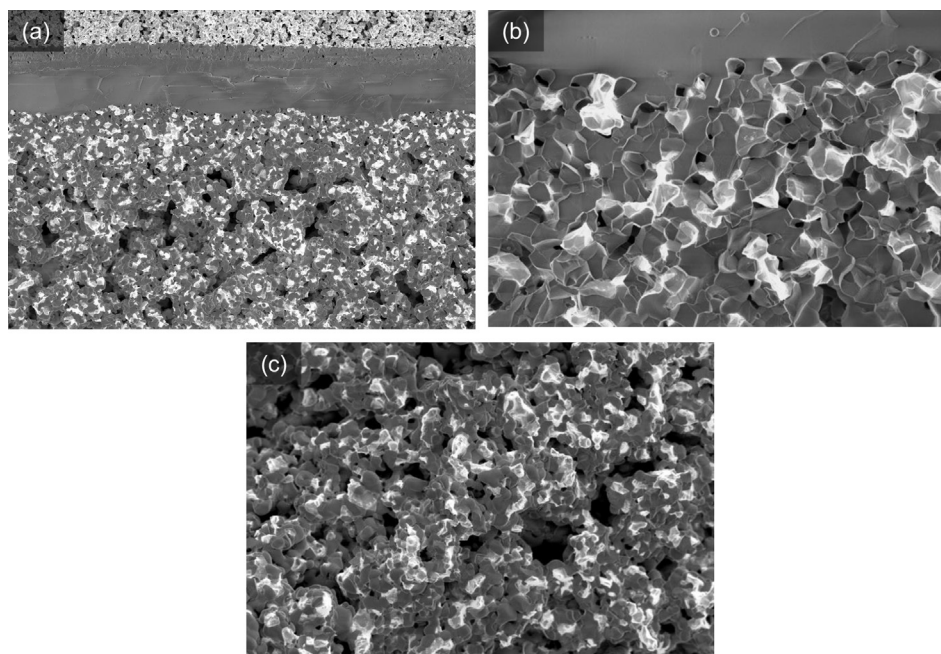


**Fig. 3.** SEM images of (a) a cross section giving all layers of ASC cell, (b) a detail of the interface between 8YSZ electrolyte and a Ni/YSZ anode functional layer, and (c) a detail of the anode substrate (type A). Material contrast is given by an in-lens detector and associated to Ni (white), YSZ (gray) and pores (dark).

and SEM imaging. While most of the reconstructions reported in literature used the in-lens detector for imaging, we found that a small number of isolated pores were not fully infiltrated by the resin and were subsequently charged during in-lens detector imaging. This phenomenon was also observed by other groups [12]. Charged areas appear very bright in the SEM images, as indicated by red arrows in Fig. 5, which seriously interferes with an automated segmentation. The SEM images revealed that these isolated pores appear more frequently inside the fine grained and less

porous AFL, which has not been analyzed in the previous reconstruction studies. As our study analyzed (for the first time) the AFL in total thickness as well as the adjacent anode substrate, we subjected both regions to a SE2 (Everhart–Thornley) detector with 1.3 keV electron beam energy.

On the downside, the SE2 detector shows a weaker contrast between the phases compared with the in-lens detector, which is particularly challenging for the image segmentation. Therefore, in the next paragraph a newly developed algorithm is presented,

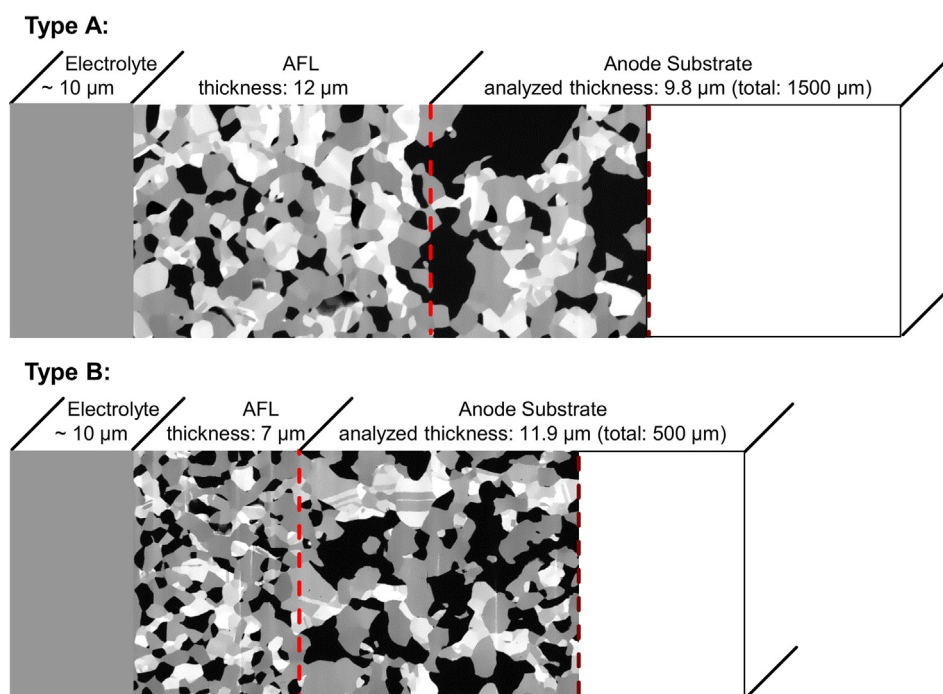


**Fig. 4.** Double-layer anode structures of anode-supported cells: type A shows an anode functional layer of 12  $\mu\text{m}$  and an anode substrate of 1500  $\mu\text{m}$ . For type B they are 7  $\mu\text{m}$  and 500  $\mu\text{m}$ , respectively. Material contrast is given by an SE2 (Everhart–Thornley) detector and associated to Ni (white), YSZ (gray) and pores (dark).



**Table 2**

Two anode-supported cells with anode functional layers (AFL) and anode substrate differing in thickness, which are reconstructed and quantified in this work.

Sample	$l_{\text{AFL}}$	$l_{\text{sub}}$	Treatment before FIB-analysis
Type A	12 $\mu\text{m}$	1500 $\mu\text{m}$	$\sim 300$ h, $T_{\text{op}} = [650\text{--}850\text{ }^{\circ}\text{C}]$
Type B	7 $\mu\text{m}$	500 $\mu\text{m}$	Only reduction at 800 $^{\circ}\text{C}$

which is able to accurately segment even in images showing a relatively low contrast between the phases.

However, an important aspect of FIB-tomography is the resolution of the FIB/SEM data, which is directly correlated to the particle size. In a previous work [28] we have shown, that a minimum of 10 pixels per particle-diameter is essential for accurately modeling the surface area  $a$  and the material fraction. In the present study, the cross-sectional resolution (pixel size of SEM images;  $x$ – $y$  plane) is 30 nm for both data sets. Accordingly, the spacing between the images (in  $z$ -direction) was also chosen to be 30 nm. For the reconstruction, 277 and 149 cross-sectional images were used for type A and type B, respectively. In total, the reconstructed volumes of the two types of anode represent sectors of  $21.78 \times 9.75 \times 8.31\text{ }\mu\text{m}^3$  and  $18.9 \times 10.5 \times 4.47\text{ }\mu\text{m}^3$ , respectively.

### 2.3. Data processing

An accurate pre-processing of the consecutive SEM images collected during FIB milling is essential for the quality of the reconstruction. The accuracy of the alignment procedure, which compensates for both, stepwise and random shift of the individual slices, is extremely important and was done using “ImageJ” [30].

After cutting-out the region of interest and aligning the generated images, an anisotropic diffusion filter was applied to the images in order to reduce the noise. This filtering is advantageous for segmentation with the newly presented *region-growing* algorithm, as it reduces the high frequency noise, while the boundaries of the particles are retained.

### 3. Phase segmentation with a *region-growing* algorithm

Segmentation of the consecutive SEM images, to our understanding, is one of the most critical steps during the reconstruction

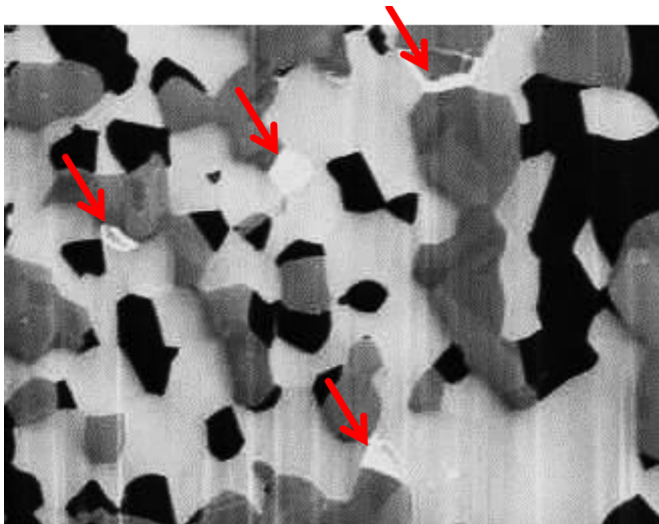


**Fig. 5.** FIB polished SEM image of the AFL region (anode-supported cell type B). Imaging by in-lens detector reveals isolated pores. These are charged and appear very bright, as indicated by (red) arrows, which seriously interferes with automated image segmentation.

process. Each and every single image consists of different grayscale values, discriminated from a value of 0 (black) to a value of 255 (white). In general, the three phases Ni, YSZ, and pore can be distinguished by their brightness values. Thereby, an automated method for the accurate segmentation of consecutive images is immensely desirable, as segmentation “by hand” is extremely time consuming and not practical for large volumes with millions of voxels (cf. Table 1).

The most common method for segmentation of pixel- and voxel-based data is using a threshold value [23]: all voxels having a grayscale value within a certain range can be partitioned into the same segment. Finding the right threshold value is a big challenge and also a large source of error, as it has a significant influence on the calculated parameters. We already discussed this aspect in detail for LSCF cathodes [19].

Naturally, the use of a threshold requires high quality image data. For example, the brightness values for the different phases must be clearly distinguishable. Poor image contrast leads to a histogram (cf. Fig. 6) where peaks tend to overlap, which makes it difficult to separate the different phases. Even more serious are “image shadowing artifacts” [20,23], which lead to images that appear lighter at one side and darker at the other, or equivalently a brightness gradient between the consecutive images.

The histogram in Fig. 6 indicates that the pore phase is easily separable by a threshold value, but the grayscale values of Ni and YSZ overlap. Applying a single threshold would lead to distortions in parameters like surface area and triple-phase boundary density. Fig. 7a shows a FIB polished SEM image of the anode functional layer (left) and part of the anode substrate (right) of sample type B. Fig. 7b shows the same region, but after a threshold segmentation. The areas marked by an oval contain many incorrectly assigned pixels, either YSZ (gray) in a large Ni (white) matrix or vice versa. The area marked by a square is magnified in Fig. 7c, and indicates an even greater problem caused by threshold segmentation.

The border between areas with dark grayscale values, assigned to the pore phase here, and areas with bright grayscale values, assigned to the Ni phase here, always contains a natural grayscale gradient of intermediate grayscale values between the dark and bright areas. By applying threshold segmentation, this small gradient between dark and light areas is erroneously assigned to the phase with the intermediate grayscale values, which is also described in Ref. [21]. Consequentially, a thin layer of YSZ is generated at the borderline between the pore phase and the Ni

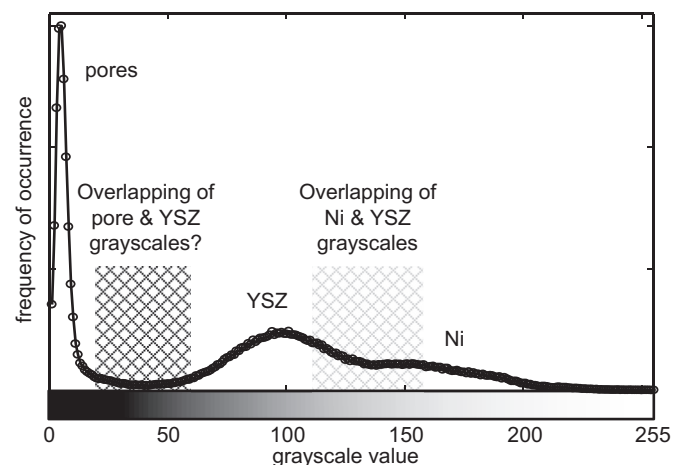


**Fig. 6.** Histogram with the grayscale frequency distribution between 0 (black) and 255 (white) given for one SEM image of sample type A. The grayscale values for the pore phase (dark) are separable from the two solid phases YSZ and Ni, whereas the brightness values for Ni and YSZ partly overlap.

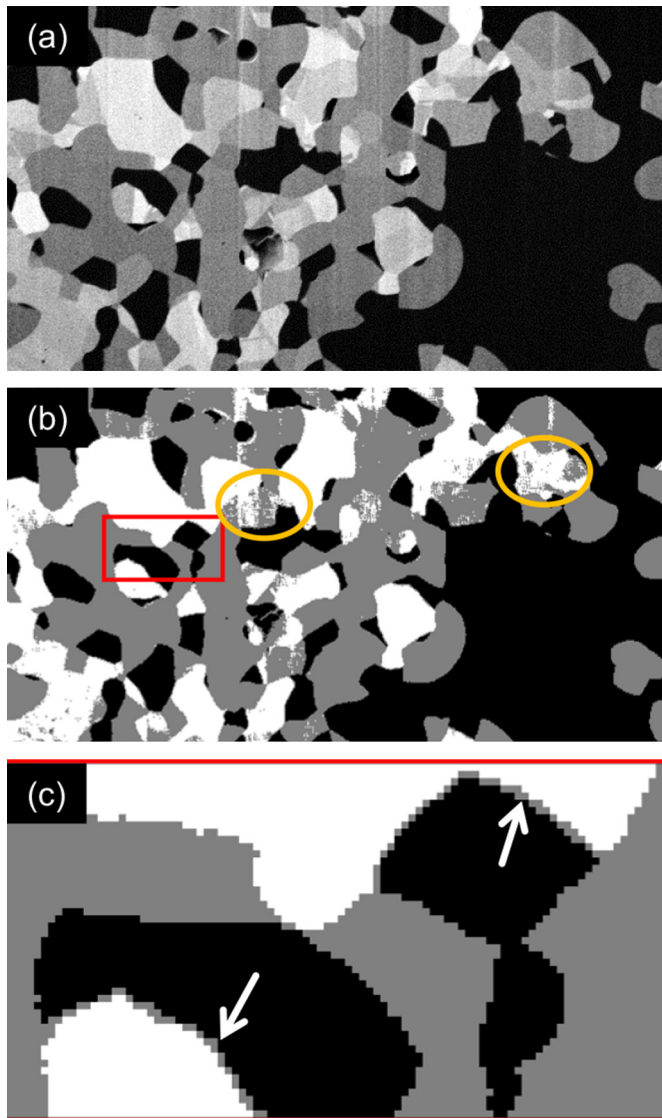


**Fig. 7.** (a) FIB polished SEM image of the anode functional layer (left) and the anode substrate (right) (ASC type A). Imaging by SE2 detector reveals the overlap of brightness values of Ni and YSZ. Please compare with the histogram in Fig. 5. (b) Same region, but after a threshold segmentation. The areas marked by an oval contain many incorrectly assigned pixels, either YSZ (gray) in a large Ni (white) matrix or vice versa, which is due to the overlap of brightness values as illustrated in the histogram. (c) Arrows indicate a thin layer of YSZ, generated at the borderline between the pore phase and the Ni phase. As a consequence, triple-phase boundaries are indiscernible and surface areas are either over- (YSZ) or underestimated (surface between nickel and pore).

phase (see arrows in Fig. 7c). As a further consequence, triple-phase boundaries are undiscoverable and surface areas are either over- (YSZ) or underestimated (surface between nickel and pore). These problems might be solved by a combination of thresholding and morphological operations [20]. This task has to be performed very carefully without changing the shape of the remaining microstructure. As a general statement, a segmentation algorithm that works perfectly for all possible microstructures does not currently exist [22].

In order to avoid errors introduced by threshold segmentation and to achieve an accurate segmentation of our data, we developed a segmentation algorithm inspired by Ref. [20], which belongs to the *region-growing* image segmentation methods [22]. The basic idea of region-growing, applied in our algorithm, is straight forward: starting from a set of voxels which we can say with certainty

belong to a specific phase (the so called “seeds”), this subset of voxels is growing according to certain requirements, until all voxels are identified. Thereby, the algorithm performs the segmentation of all three phases simultaneously in 3D.

However, before starting the segmentation a preprocessing step is necessary. The boundaries between the phases (which can be interpreted as edges inside the data set) are detected with an edge detection filter and all voxels belonging to an edge are labeled as “edge”. This information is stored in a so-called “*edge-map*”, which is settled here using the Canny-algorithm [31].

Then, all voxels that are very likely to belong to a certain phase are set as a starting point (“seed”). These seeds can be identified, for example, by a careful inspection of the histogram. In this instance; the seeds for the pore phase would be a small subset of voxels with a very low intensity (e.g. grayscale values  $< 25$ , cf. Fig. 8). In contrast, the seeds for the Ni phase would be voxels with a high intensity that are especially different to those of the YSZ phase (e.g. grayscale values  $> 170$ ). In addition, the seeds for the YSZ phase should be chosen in such a way that the intensity is high enough so as to not belong to the pore phase, but low enough as to not belong to the Ni phase (e.g. grayscale values in-between 70 and 100 in Fig. 8). Moreover, the absence of a grayscale gradient in the neighborhood of the Ni phase seed should be assured, as this indicates the gradient between the dark pore phase and the bright YSZ phase.

For an automated identification of the seeds, we first divide the histogram shown in Fig. 8 into three sections by two classical segmentation methods. For the structures investigated here, we consider Otsu’s method [32] to be most suitable for separation of pore and YSZ, and maximum entropy [33] for the separation of YSZ and nickel. As a consequence, threshold calculations have to be performed separately for every single image, as the consecutive images quite often have a gradient in grayscale values. These gradients do not appear with the same distinctness for the different phases, as the pore phase is nearly unaffected while YSZ can show pronounced gradients. To overcome this constraint, we chose to interpolate the obtained threshold values linearly, which is advantageous, as the resulting data do not contain any discontinuities. We confirmed the correctness of our segmentation procedure by a subsequent EDX analysis of the last image.

The second step is the iterative growing process. Spreading out from the seeds, all “not yet assigned” neighboring voxels which have a joint surface with one of the seed-voxels are checked to determine if they belong to the same phase. If a voxel is assigned the same phase, this voxel is added to the seed and the next iteration step is started. As a general rule, growing across edges is not allowed, which is controlled by using the *edge-map*. However, growing of the phases requires additional rules which cooperatively identify where the growth of a specific phase ends. Altogether, four decision criteria are established:

- (1) Growing across edges is not allowed, which is controlled by using the *edge-map*.
- (2) Probability that the grayscale value of the approached voxel still belongs to the phase - uncertainties are highest on or near the threshold values.
- (3) Gradient in grayscale values of two neighboring voxels, namely between seed-voxel and considered voxel – the smaller the difference, the greater the probability that they belong to the same phase
- (4) Number of neighboring voxels already assigned to the three possible phases – the more neighboring voxels belong to phase  $i$ , the more likely it is that this voxel also belongs to phase  $i$

These criteria can be weighted according to the requirements and the image data quality. For example: (i) criteria (2) should

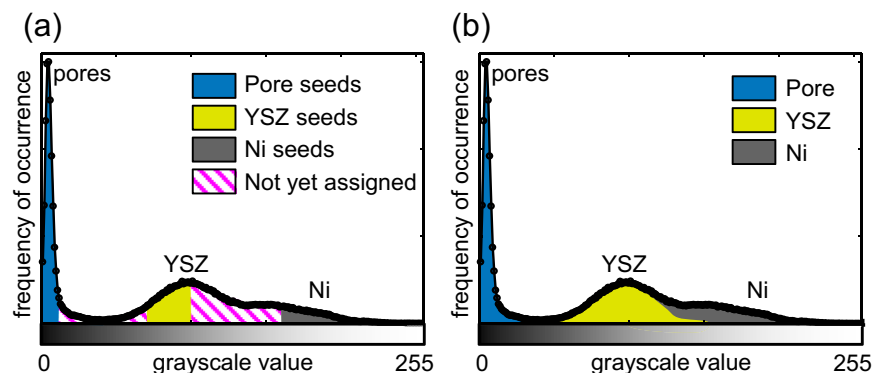


**Fig. 8.** Region-growing algorithm: (a) schematic histogram at the start of the segmentation procedure, with grayscale values assigned to seeds of the pore phase (blue), YSZ phase (yellow), and Ni phase (gray). (b) Schematic histogram at the end of the segmentation procedure showing the assignment to pore phase, YSZ phase and Ni phase. (For interpretation of the references to color in this figure legend, the reader is referred to the web version of this article.)

have the highest weight, if the brightness values of all phases are clearly separable, (ii) criteria (4) should have a higher weight, if the brightness values of the phases are close to each other. Additionally, the weight of criteria (1)–(4) can vary during the segmentation process of a large image data set. Assigning voxels with a grayscale value on or near one of the two threshold values is most critical, as they have the same probability of belonging to both phases. In these critical areas, all four criteria will be taken into account. In contrast, the first two criteria are sufficient for voxels with a grayscale value which is far away from the thresholds. As mentioned before, all phases grow simultaneously and the iterative process of segmentation is completed, if all voxels of the FIB/SEM data set are assigned to one of the three phases.

The third step is a morphological operation, which is only performed optionally after the growing process. This step is necessary in a few cases, as shown in Fig. 7c, where arrows indicate a thin layer of YSZ, generated erroneously at the borderline between the pore phase and the Ni phase. By the morphological operation, all phases shrink together just to expand later, removing these slim regions. This reassignment re-applies the four criteria of the growing process.

As a strong point, our region growing algorithm considers both, information on grayscale values and geometrical information like boundaries and gradients between two adjacent phases. This approach results in a more reliable separation result, especially for images showing low contrast between the phases. For example, the watershed method results in an overestimation of the Ni phase, which is amplified for image data showing noise effects.

As a weak point, our region growing algorithm requires the definition of robust “seeds” at the beginning of the region growing process. Like for almost all other segmentation methods, the appearance of twin boundaries in the Ni phase – which can often be seen using low energy imaging (e.g. in Fig. 4 inside the substrate of sample type B) – is causing difficulties. The Canny algorithm will detect an edge inside the nickel grain, which may affect the segmentation result. For our region growing algorithm, two cases are probable: (i) a correct result if Ni seeds are detected on both sides of the twin boundary, (ii) an incorrect result if a Ni seed and a pore or YSZ seed are detected. In this case, the phase assignment has to be corrected manually.

We developed this *region-growing* algorithm for anodes, as they usually consist of three phases. However, this algorithm has the potential to be applied for the segmentation of more phases, or on electrodes made of two phases.

#### 4. Results and discussion

The reconstruction data sets of type A and type B cells were now utilized for calculating the following microstructural parameters of the anode functional layer and the anode substrate separately:

(1) material/porosity fraction  $X_i$ , (2) phase connectivity, (3) triple-phase boundary density  $l_{TPB}$ , (4) volume-specific surface area  $A_i$  and, (5) “particle sizes”  $ps_i$  of Ni, YSZ, and pore phase.

The reconstructed volumes of the double-layer anodes have a total size of  $1765 \mu\text{m}^3$  for type A and  $887 \mu\text{m}^3$  for type B and are shown in Fig. 9. These volumes are subdivided into a sector for the anode functional layer, which has a volume of  $972 \mu\text{m}^3$  for type A

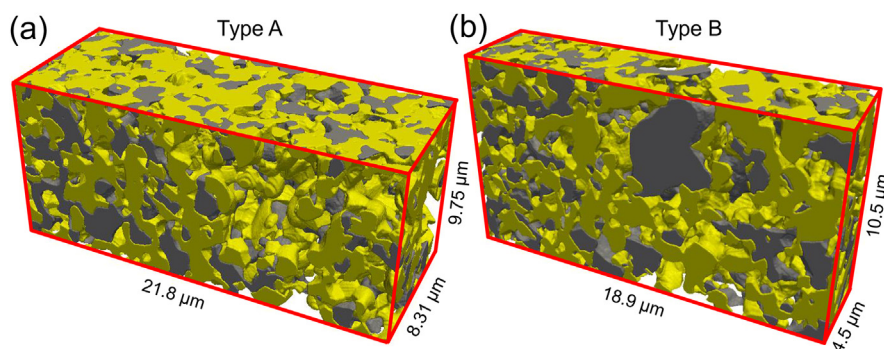


**Fig. 9.** Total reconstructed volumes of the 2 types of double-layer anodes,  $1765 \mu\text{m}^3$  for type A and  $887 \mu\text{m}^3$  for type B. The anode functional layer is on the left side, the anode substrate on the right. Ni grains are colored in dark-gray and YSZ grains in yellow, whereas pores are left out for reasons of simplification. (For interpretation of the references to color in this figure legend, the reader is referred to the web version of this article.)



**Table 3**

Volume fractions  $X_i$  (in %) of the individual phases calculated for AFL and anode substrate.

	AFL type A	AFL type B	Anode substrate type A	Anode substrate type B
$X_{Ni}$ [%]	29.4	28.5	19.5	24.6
$X_{YSZ}$ [%]	48.5	49.3	38.2	41.4
$X_{pore}$ [%]	22.3	22.2	42.3	34.0

and of  $328 \mu\text{m}^3$  for type B. For the anode substrate, the volume investigated is  $792 \mu\text{m}^3$  for type A and  $559 \mu\text{m}^3$  for type B.

The volume sizes are believed to be large enough to provide good statistics, as Wilson et al. [34] found an error of 2% for volumes  $\geq 500 \mu\text{m}^3$  of composite electrodes. However, a detailed comparison of the microstructure parameters of type A and type B are not in the focus of this study, as both ASCs have a different prehistory (see Table 2). During operation, the anode microstructure changes, depending on experimental conditions [14]. In the following subsections, the results of the calculated material parameters are presented.

#### 4.1. Volume fraction

The most fundamental characteristic of a composite electrode is the volume fraction  $X_i$  of each individual phase  $i$ . These values are calculated by dividing the number of voxels assigned to the specific phase by the total number of voxels. The results for Ni, YSZ and pore phase within the anode functional layer and the anode substrate are summarized in Table 3.

The volume fraction of the pore phase is 22.3% and 22.2% in both anode functional layers and thus very similar. As expected, the porosity of the substrate is much higher, but differs significantly among both substrates. The type A substrate porosity of 42.3% is almost twice as high compared to the AFL with 22.3%. In our opinion, this porosity effectively compensates for a higher gas diffusion polarization in the  $1500 \mu\text{m}$  thick substrate. Its contribution was reported as  $\leq 20 \text{ m}\Omega \text{ cm}^2$  at a simulated fuel utilization of 65% and for temperatures between  $550^\circ\text{C}$  and  $850^\circ\text{C}$  for a structurally and chemically similar ASC [27].

#### 4.2. Phase connectivity

The connectivity of Ni, YSZ and pore phase is calculated using MATLAB (The MathWorks, Natick, MA, USA) by labeling all clusters of voxels as

- (1) *isolated* within the reconstructed volume,
- (2) *unknown*, i.e. they appear isolated but intersect one of the outer boundaries in a way in the portion outside the measured volume has unknown connectivity or they are connected only by an edge or vertex
- (3) *connected*, for voxels of YSZ if percolating with the electrolyte; Ni if percolating with the current collector and pores with the gas channel.

**Table 4**

Percentage of *connected* ( $c$ ), *unknown* ( $u$ ) and *isolated* ( $i$ ) voxels for the individual phases, calculated separately for the AFL and for the anode substrate, respectively.

	AFL type A			AFL type B			Anode substr. type A			Anode substr. type B		
	$c$	$u$	$i$	$c$	$u$	$i$	$c$	$u$	$i$	$c$	$u$	$i$
Connected Ni [%]	98.2	0.7	1.1	98.5	1.1	0.4	97.2	1.8	1.0	94.8	4.2	1.0
Connected YSZ [%]	99.9	0.0	0.1	99.9	0.0	0.1	99.7	0.2	0.1	99.3	0.5	0.2
Connected Pore [%]	76.8	17.3	5.9	77.6	14.0	8.4	98.6	0.6	0.8	96.9	2.7	0.4

Thereby only neighboring voxels of the same phase which share a common face were considered as connected. However, in literature sometimes also voxels are defined as connected, if they only share a common edge or even only a vertex. Nevertheless, the results of the connectivity analysis should be similar, irrespective of the definition of connectivity, which is the case for our reconstructions. If not, a significant number of particles would only be connected via voxel-vertices and not also via voxel-faces. This in turn indicates that the image resolution should be increased to resolve the connection between the particles more accurately. The percentage of *connected* ( $c$ ), *unknown* ( $u$ ) and *isolated* ( $i$ ) voxels is given in Table 4 for the individual phases. Moreover, the results of the connectivity analysis are visualized in Fig. 10. The percentage of isolated pore phase is very low in both substrates, namely 0.8% in type A and 0.4% in type B, but increases inside the AFL to 5.9% and 8.4%, respectively.

The connectivity of the two solid phases, Ni and YSZ, and of the pore phase in both substrates is  $\geq 94.8\%$ , while it is much lower inside AFLs. This is related to the lower value of porosity (cf. Table 3), as the probability that all pores are connected is decreasing. The relatively high number of voxels with an *unknown* connectivity status is mainly related to sample geometry, as in the image slicing direction the length is only  $8.3 \mu\text{m}$  for type A and  $4.5 \mu\text{m}$  for type B. In a forthcoming work, more images will be used for the reconstruction and hence a greater and more cubic volume will be taken into account.

As all voxels are now labeled with their connectivity status, this information can be combined with the calculation of the TPB in order to identify potentially active and non-active TPBs.

#### 4.3. Triple-phase boundary density

The calculated triple-phase boundary density  $l_{TPB}$  is normalized to the sample volume. This parameter is of particular importance for the electrochemical performance of the anode, as the oxidation reaction occurs at the TPB between Ni, YSZ and pore phase. Different methods for calculating  $l_{TPB}$  are given in literature, and a short overview is to be found in Ref. [10]. This study applies the centroid method, as introduced by Shikazono et al. [9], and the results are listed in Table 5. In addition, the TPB was calculated directly from the voxel mesh by a simple edge summation. This second method leads to much higher values ( $\sim 1.56$  times higher) compared to the centroid method, where the TPB is much more “smoothed” and hence more realistic. The factors which link the values obtained by the two methods are also listed in Table 5. The huge difference between these values clearly shows the necessity of applying appropriate methods. Moreover it impedes a comparison of literature data.

As desirable, the  $l_{TPB, total}$  in the AFL is highest with  $2.56 \mu\text{m}^{-2}$  for type A and  $4.36 \mu\text{m}^{-2}$  for type B. For an anode similar to type A,  $l_{TPB, total}$  of  $2.56 \mu\text{m}^{-2}$  is tied up with an area specific resistance of  $35 \text{ m}\Omega \text{ cm}^2$  at  $800^\circ\text{C}$  and  $<1.5 \Omega \text{ cm}^2$  at  $550^\circ\text{C}$  at a fuel utilization of 65% for the oxidation reaction [27]. It is to be expected, that the AFL of type B performs even better because  $l_{TPB, total}$  is considerably larger.



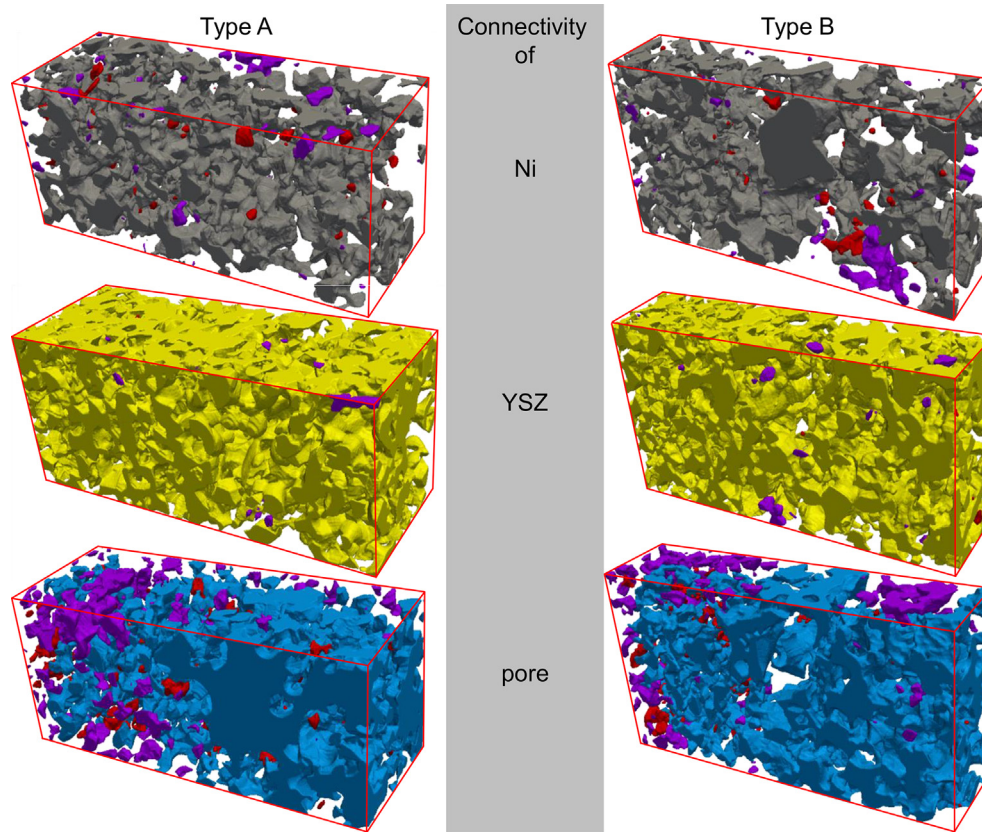


**Fig. 10.** Results of the connectivity analysis of the different phases for type A (left) and type B (right), respectively: red represents isolated parts, violet represents parts of unknown status, whereas the gray, yellow or blue (for Ni, YSZ or pore phase) represents parts that are connected to the left side (which is the interface to the YSZ electrolyte) for the YSZ or to the right side (which is the direction of the current collector and fuel supply, respectively) for pores and nickel.

Fig. 11 compares  $l_{\text{TPB,total}}$  of type A and type B double layer anodes as a function of the distance to the electrolyte. For this, the  $l_{\text{TPB,total}}$  is calculated for each individual slice directly by edge summation [9], starting from the AFL/electrolyte interface to the interface AFL/substrate and towards the direction of the current collector/gas channel. This analysis discloses a large difference in AFL extension between both types of anodes, as already indicated in the SEM images in Fig. 4. Type B shows a clear drop of  $l_{\text{TPB,total}}$  in a distance of 6–9  $\mu\text{m}$  from the electrolyte, which is the interface AFL/substrate. In contrast,  $l_{\text{TPB,total}}$  gives only a slight decreasing trend for type A. The interface AFL/substrate is set at a distance of 12  $\mu\text{m}$  from the electrolyte as illustrated in Fig. 4, but could possibly extend more. Interestingly enough, the lateral extension of the

electrochemical active volume was already determined in Ref. [35], to be increasing from 10  $\mu\text{m}$  at 950  $^{\circ}\text{C}$  to 14  $\mu\text{m}$  at 750  $^{\circ}\text{C}$  for a chemically similar, but structurally different type of anode. Hopefully, a critical examination of the relationship between performance and TPB length becomes tangible with the progress presented here.

#### 4.4. Volume specific surface area

The volume specific surface area  $A_i$  of all phases is calculated using the marching cube algorithm [36], which we already applied for a mixed-conducting, porous LSCF cathode for SOFC in Ref. [37]. This algorithm determines shape and area of the shared boundary

**Table 5**

Calculated triple-phase boundary densities  $l_{\text{TPB}}$  for both types of anodes, separately analyzed for AFL and anode substrate. The densities were calculated for all TPBs ( $l_{\text{TPB,total}}$ ), for TPBs where the connectivity-status of at least one of the phases is unknown ( $l_{\text{TPB,unknown}}$ ) and for inactive TPBs ( $l_{\text{TPB,isolated}}$ ), where at least one of the phases is isolated. Moreover, the  $l_{\text{TPB}}$  is calculated (1) with the centroid method [9] and (2) directly from a voxel mesh by a simple edge summation. The factor that links the two values is also listed.

		AFL type A	AFL type B	Anode substrate type A	Anode substrate type B
$l_{\text{TPB,total}} [\mu\text{m}^{-2}]$	Centroid voxel-mesh Factor	2.56	4.36	1.76	2.14
		3.94	6.79	2.71	3.33
		1.54	1.56	1.54	1.56
$l_{\text{TPB,unknown}} [\mu\text{m}^{-2}]$	Centroid voxel-mesh Factor	0.51	0.76	0.12	0.34
		0.80	1.19	0.18	0.54
		1.57	1.57	1.57	1.57
$l_{\text{TPB,isolated}} [\mu\text{m}^{-2}]$	Centroid voxel-mesh Factor	0.49	0.91	0.22	0.20
		0.75	1.41	0.34	0.31
		1.53	1.55	1.55	1.55

**Table 6**

Volume specific surface areas of the three phases for the anode functional layer and for the anode substrate for both types of anodes.

	AFL type A	AFL type B	Anode substrate type A	Anode substrate type B
$A_{\text{Ni}} [\mu\text{m}^{-1}]$	1.62	2.17	1.14	1.34
$A_{\text{YSZ}} [\mu\text{m}^{-1}]$	2.33	3.11	1.93	2.17
$A_{\text{pore}} [\mu\text{m}^{-1}]$	1.68	2.28	1.54	1.82
$A_{\text{Ni/pore}} [\mu\text{m}^{-1}]$	0.49	0.67	0.37	0.49
$A_{\text{Ni/YSZ}} [\mu\text{m}^{-1}]$	1.14	1.50	0.76	0.84
$A_{\text{YSZ/pore}} [\mu\text{m}^{-1}]$	1.20	1.61	1.16	1.33

surface, using the information of eight neighboring voxels. Table 6 summarizes the surface areas  $A_i$  obtained for Ni, YSZ and pore phase, and the surface areas between two phases  $A_{\text{Ni/pore}}$ ,  $A_{\text{YSZ/pore}}$  and  $A_{\text{Ni/YSZ}}$ .

As for the calculation of TPB density, the fact that different methods for calculating  $A_i$  are applied in literature generally impedes a comparison. The influence of the specific method on the calculated  $A_i$  values was already discussed in Ref. [37].

The volume-specific surface area  $A_{\text{Ni}}$  and the two-phase surface area  $A_{\text{Ni/pore}}$  are a measure for the accessible catalyst surface for oxidation of hydrogen and internal reforming reactions. It becomes evident, that type B with values of  $2.17 \mu\text{m}^{-1}$  and  $0.67 \mu\text{m}^{-1}$  in the AFL is superior to type A, which shows 20–30% lower values thereof. The difference among both anode substrates is less pronounced.

In general, all values of volume-specific surface areas  $A_i$  and the surface area between two phases are higher for type B when compared to type A. This suggests that the individual particles are smaller in type B anodes, and that the particles inside the AFL are

smaller when compared to the anode substrate. The particle size is analyzed in the following subsection.

#### 4.5. Particle size

The method for obtaining the particle size distributions of Ni, YSZ and pore is based on the Euclidean distance transform, which is described in detail in Ref. [38]. A distance map is calculated, which contains the information about the distance (i) between each voxel inside a particle and, (ii) to its closest outside neighbor. Hence, the centers of the particles are given by the local maxima, whereas the height of each maximum is a measure for the particle radius. Table 7 gives the median values  $ps_i$  (particle diameter) and Fig. 12 the particle size distributions (diameters) of the three phases.

First, the median pore size  $ps_{\text{pore}}$  and the pore size distribution between type A and type B anodes are significantly different, both in the AFL and in the anode substrate. For type B, median pore size in the anode substrate and in the AFL is  $\sim 15$ –22% smaller compared to type A. The pore size distribution in Fig. 12 shows, that the pore size becomes as large as  $2.5 \mu\text{m}$  in the anode substrate of type A and as large as  $1.5 \mu\text{m}$  for type B. In agreement with the inspection of SEM images (cf. Fig. 4), the pore sizes are sufficiently large for low-loss gas diffusion from the gas channel to the AFL. For an anode substrate similar to type A, an area specific resistance of  $20 \text{ m}\Omega \text{ cm}^2$  at  $850^\circ\text{C}$  and  $15 \text{ m}\Omega \text{ cm}^2$  at  $550^\circ\text{C}$  at a fuel utilization of 65% for the gas diffusion polarization was reported in Ref. [27].

Furthermore, for type A it is anticipated that the powder quality of Ni and YSZ is the same for AFL and anode substrate, as the median particle size for Ni is  $0.538 \mu\text{m}$  and  $0.541 \mu\text{m}$ , and for YSZ is  $0.623 \mu\text{m}$  and  $0.629 \mu\text{m}$ . For the type B anode, Ni as well as YSZ particles inside the AFL are by 17.5% and 20% smaller compared to the substrate. Furthermore, smaller particle sizes in the AFL are associated with higher TPB density and surface areas when compared to the values calculated for type A.

## 5. Conclusions

Performance characteristics of solid oxide fuel cell anodes are tied to microstructure parameters as material fractions, surface areas, grain and pore sizes, as well as phase connectivity and triple-phase boundary density. In this work, the 3D reconstruction of double-layer Ni/YSZ anodes required the development of an advanced algorithm, based on a region-growing image segmentation method, which allowed automated grayscale segmentation even for SEM images with low contrast between the two solid phases. We state this algorithm as superior for the segmentation of three phases compared to the standard threshold segmentation. Furthermore, this method is supportive for the segmentation of grayscale data obtained by methods other than FIB/SEM tomography and has the potential to be applied for the segmentation of more than three phases.

In this contribution, two types of high-performance Ni/YSZ anodes – differing in thickness of the anode functional layer and the anode substrate – are reconstructed and compared to each other.

**Table 7**

Particle sizes  $ps_i$  (particle diameter) of Ni and YSZ and the pore sizes within anode functional layer (AFL) and anode substrate for ASC type A and type B. The listed values represent the median (and mean values in parentheses) of the calculated particle size distribution (cp. Fig. 11).

	AFL type A	AFL type B	Anode substrate type A	Anode substrate type B
$ps_{\text{Ni}} [\mu\text{m}]$	0.538 (0.560)	0.407 (0.430)	0.541 (0.560)	0.493 (0.526)
$ps_{\text{YSZ}} [\mu\text{m}]$	0.623 (0.627)	0.464 (0.486)	0.629 (0.633)	0.592 (0.604)
$ps_{\text{pore}} [\mu\text{m}]$	0.483 (0.495)	0.378 (0.382)	0.641 (0.809)	0.541 (0.580)

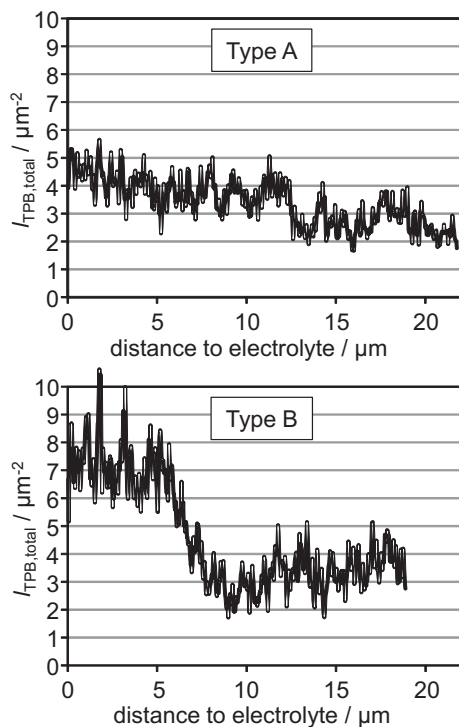


**Fig. 11.** Distribution of total TPB density  $l_{\text{TPB,total}}$ , calculated from the AFL/electrolyte interface towards the current collector/gas channel, thus showing the decrease of  $l_{\text{TPB,total}}$  from the AFL into the substrate. Note:  $l_{\text{TPB,total}}$  is calculated directly from the voxel mesh by a simple edge summation for each individual slice of the investigated layer separately (cf. Table 5).

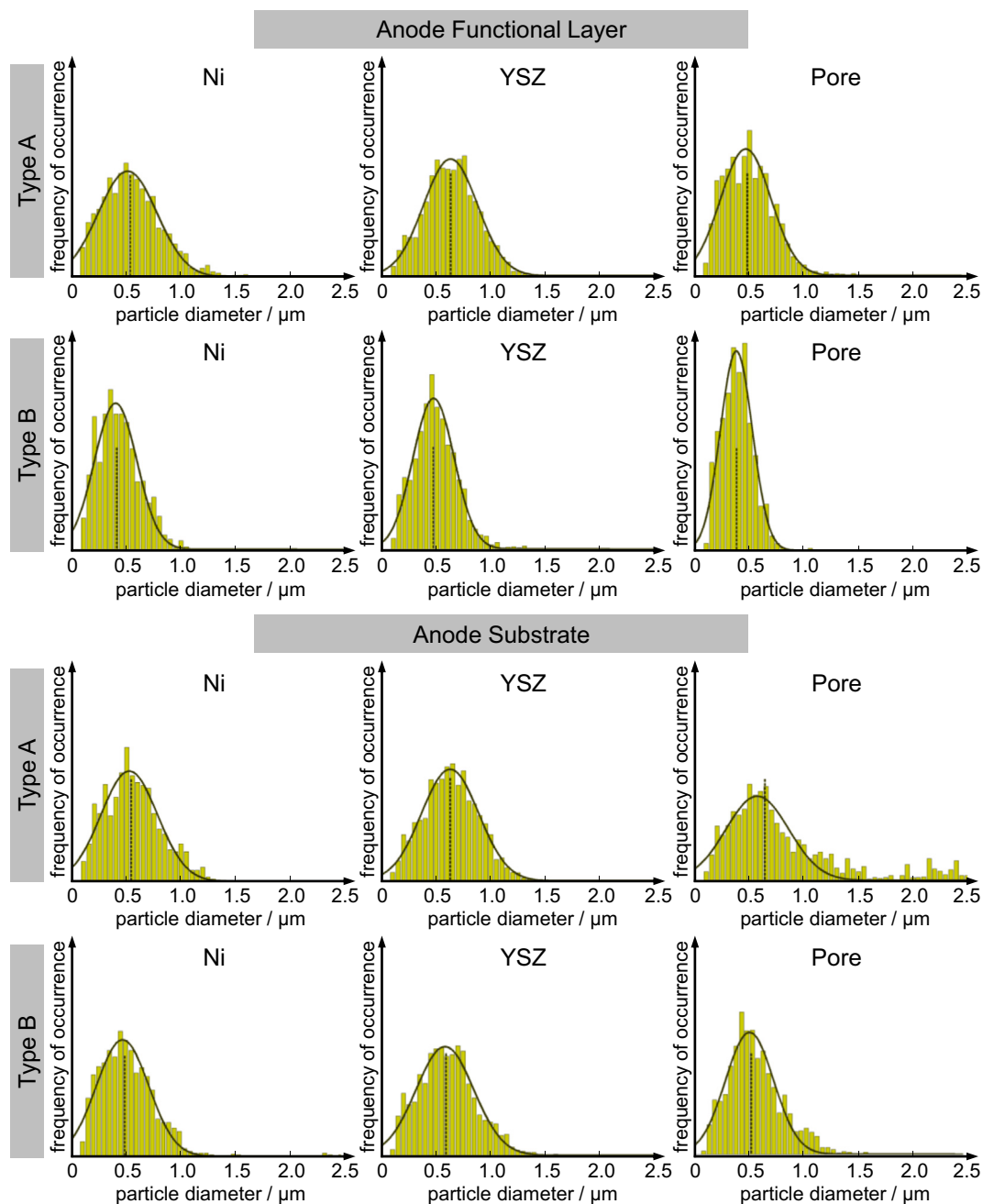


**Fig. 12.** Particle size distribution of AFL and substrate, calculated for both types of anodes. The dotted lines indicate the median values of the given distributions (see Table 7), while the curved line shows an approximation of the distribution by a Gaussian function.

For the first time, the anode functional layer adjacent to the thin film electrolyte is separately quantified.

One of the most apparent differences between the AFL and the anode substrate are the material and porosity fractions. For example, a much higher content of porosity (42.3% for type A and 34.0% for type B, respectively) has been detected in the substrate compared to the AFL (22.3% for type A and 22.2% for type B, respectively). For both types of anode, especially inside the AFL, the phase connectivity of the pore phase was found to be 21.4–23.1% smaller than for nickel and YSZ, due to the small amount of porosity.

As expected, the median pore size was found to be much bigger inside the substrate than inside the AFL (0.641 μm inside the

substrate and 0.483 μm inside the AFL for type A and 0.541 μm inside the substrate and 0.378 μm inside the AFL for type B). While the nickel and YSZ particles are nearly the same in both layers for type A, these particles were found to be up to 22% bigger inside the anode substrate compared to the AFL for type B. Moreover, the particles inside the AFL of type B are smaller compared to the AFL of type A (e.g. particle size of YSZ is 0.464 μm for type B and 0.623 μm for type A, respectively).

However, the two types of anodes differ most in the triple-phase boundary density, which is the key property for high-performance. While for type A the total TPB density is  $2.56 \mu\text{m}^{-2}$  in the anode functional layer, these values increase for type B to  $4.36 \mu\text{m}^{-2}$ , which is larger by more than 50%.

## Acknowledgments

The authors would like to thank Dr. Thomas Carraro from the University of Heidelberg and undergraduate students Andreas Messner, Anne Wannenwetsch and Christine Dörflinger from the Karlsruher Institut für Technologie (KIT) for their invaluable support of this work. This work was funded by the Friedrich-und-Elisabeth-BOYSEN-Stiftung and by the Deutsche Forschungsgemeinschaft (DFG) through the project “Modellierung, Simulation und Optimierung der Mikrostruktur mischleitender SOFC-Kathoden” (IV 14/16-1, RA 306/17-1). Further support by the DFG through the Center for Functional Nanostructures (CFN) is gratefully acknowledged.

## References

- [1] E. Ivers-Tiffée, W. Wersing, M. Schießl, *Berichte der Bunsengesellschaft Physikalische Chem.* 94 (1990) 978–981.
- [2] A. Atkinson, S.A. Barnett, R.J. Gorte, J.T.S. Irvine, A.J. McEvoy, M. Mogensen, S.C. Singhal, *Nat. Mater.* 3 (2004) 17–27.
- [3] W.G. Bessler, M. Vogler, H. Störmer, D. Gerthsen, A. Utz, A. Weber, E. Ivers-Tiffée, *Phys. Chem. Chem. Phys.* 12 (2010) 13888–13903.
- [4] P.R. Shearing, J. Golbert, R.J. Chater, N.P. Brandon, *Chem. Eng. Sci.* 64 (2009) 3928–3933.
- [5] D. Kanno, N. Shikazono, N. Takagi, K. Matsuzaki, N. Kasagi, *Electrochim. Acta* 56 (2011) 4015–4021.
- [6] P.R. Shearing, Q. Cai, J.I. Golbert, V. Yufit, C.S. Adjiman, N.P. Brandon, *J. Power Sources* 195 (2010) 4804–4810.
- [7] J.R. Wilson, W. Kobsiriphat, R. Mendoza, H.Y. Chen, J.M. Hiller, D.J. Miller, K. Thornton, P.W. Voorhees, S.B. Adler, S.A. Barnett, *Nat. Mater.* 5 (2006) 541–544.
- [8] K. Matsuzaki, N. Shikazono, N. Kasagi, *J. Power Sources* 196 (2011) 3073–3082.
- [9] N. Shikazono, D. Kanno, K. Matsuzaki, H. Teshima, S. Sumino, N. Kasagi, *J. Electrochem. Soc.* 157 (2010) B665–B672.
- [10] H. Iwai, N. Shikazono, T. Matsui, H. Teshima, M. Kishimoto, R. Kishida, D. Hayashi, K. Matsuzaki, D. Kanno, M. Saito, H. Muroyama, K. Eguchi, N. Kasagi, H. Yoshida, *J. Power Sources* 195 (2010) 955–961.
- [11] N. Vivet, S. Chupin, E. Estrade, T. Piquero, P.L. Pommier, D. Rochais, E. Bruneton, *J. Power Sources* 196 (2011) 7541–7549.
- [12] J.S. Cronin, J.R. Wilson, S.A. Barnett, *J. Power Sources* 196 (2011) 2640–2643.
- [13] M. Kishimoto, H. Iwai, M. Saito, H. Yoshida, *J. Power Sources* 196 (2011) 4555–4563.
- [14] T. Matsui, J.Y. Kim, H. Muroyama, M. Shimazu, T. Abe, M. Miyao, K. Eguchi, *Solid State Ionics* 225 (2012) 50–54.
- [15] T. Matsui, R. Kishida, J.-Y. Kim, H. Muroyama, K. Eguchi, *J. Electrochem. Soc.* 157 (2010) B776–B781.
- [16] J. Laurencin, R. Quey, G. Delette, H. Suhonen, P. Cloetens, P. Bleuet, *J. Power Sources* 198 (2012) 182–189.
- [17] P.R. Shearing, J. Gelb, N.P. Brandon, *J. Eur. Ceramic Soc.* 30 (2010) 1809–1814.
- [18] T. Carraro, J. Joos, B. Rüger, A. Weber, E. Ivers-Tiffée, *Electrochim. Acta* 77 (2012) 315–323.
- [19] J. Joos, T. Carraro, A. Weber, E. Ivers-Tiffée, *J. Power Sources* 196 (2011) 7302–7307.
- [20] P.S. Jorgensen, K.V. Hansen, R. Larsen, J.R. Bowen, *Ultramicroscopy* 110 (2010) 216–228.
- [21] L. Holzer, B. Iwanschitz, Th. Hocker, B. Münch, M. Prestat, D. Wiedenmann, U. Vogt, P. Holtappels, J. Seifr, A. Mai, Th. Gaule, *J. Power Sources* 196 (2011) 1279–1294.
- [22] J.P. Simmons, P. Chuang, M. Comer, J.E. Spowart, M.D. Uchic, M. De Graef, *Model. Simul. Mater. Sci. Eng.* 17 (2009).
- [23] L. ÓGorman, M.J. Sammon, M. Seul, *Practical Algorithms for Image Analysis*, Cambridge University Press, Cambridge, 2008.
- [24] L. Holzer, B. Münch, B. Iwanschitz, Th. Hocker, M. Cantoni, Th. Gaule, *J. Power Sources* 196 (2011) 1279–1294.
- [25] A. Leonide, V. Sonn, A. Weber, E. Ivers-Tiffée, *J. Electrochem. Soc.* 155 (2008) B36–B41.
- [26] C. Endler, A. Leonide, A. Weber, F. Tietz, E. Ivers-Tiffée, *J. Electrochem. Soc.* 157 (2010) B292–B298.
- [27] E. Ivers-Tiffée, J. Hayd, D. Klotz, A. Leonide, F. Han, A. Weber, *ECS Trans.* 35 (2011) 1965–1973.
- [28] J. Joos, M. Ender, T. Carraro, A. Weber, E. Ivers-Tiffée, *Electrochim. Acta* 82 (2012) 268–276.
- [29] T. Kanit, S. Forest, I. Galliet, V. Mounoury, D. Jeulin, *Int. J. Solids Struct.* 40 (2003) 3647–3679.
- [30] W.S. Rasband, *Image J*, National Institutes of Health, Bethesda, Maryland, USA, U. S., 1997. Ref type: Computer program.
- [31] J. Canny, *IEEE Trans. Pattern Anal. Machine Intell.* 8 (1986) 679–698.
- [32] N. Otsu, *IEEE Trans. Syst. Man Cybern.* 9 (1979) 62–66.
- [33] J.N. Kapur, P.K. Sahoo, A.K.C. Wong, *Comput. Vis. Graph. Image Process.* 29 (1985) 273–285.
- [34] J.R. Wilson, J.S. Cronin, A.T. Duong, S. Rukes, H.Y. Chen, K. Thornton, D.R. Mumm, S. Barnett, *J. Power Sources* 195 (2010) 1829–1840.
- [35] V. Sonn, A. Leonide, E. Ivers-Tiffée, *J. Electrochem. Soc.* 155 (2008) B675–B679.
- [36] W.E. Lorensen, H.E. Cline, *Comput. Graph.* 21 (1987) 163–169.
- [37] J. Joos, T. Carraro, M. Ender, B. Rüger, A. Weber, E. Ivers-Tiffée, *ECS Trans.* 35 (2011) 2357–2368.
- [38] M. Ender, J. Joos, T. Carraro, E. Ivers-Tiffée, *J. Electrochem. Soc.* 159 (2012) A972–A980.